World Scientific
www.worldscientific.com

Dielectric relaxation and conduction mechanism of NaMgPO$_4$ compound

L. Miladi*, A. Oueslati, M. Ben Gzaiel and M. Gargouri

Laboratory of Spectroscopic Characterization and Optical Materials, Faculty of Sciences
University of Sfax B.P. 1171, 3000 Sfax, Tunisia

*leilamiladi@yahoo.fr

The polycrystalline NaMgPO$_4$ ceramic, synthesized via a high-temperature solid-state reaction route, has been characterized by using different experimental procedures. The X-ray powder diffraction confirmed the phase formation of the synthesized compound in the orthorhombic phase. It assumed an olivine-type structure made up of corners linked between tetrahedral PO$_4$ and octahedral NaO$_6$ and MgO$_6$ groups. Infrared and Raman spectroscopies confirmed the presence of PO$_4^{3-}$ groups. Local structure and chemical bonding between MgO$_6$ octahedral and PO$_4^{3-}$ tetrahedral groups investigated by diffusion Raman is the feature in the phase transition at $T = 693$ K. The temperature dependences of the real ε' and imaginary ε'' parts of dielectric permittivity show a distribution of relaxation times. From Nyquist plots, the presence of grain and grain boundary effect in the material is noticed. The impedance spectroscopy measurement showed a non-Debye-type process. From the impedance data, the determined grain resistance reduces with increment of temperature showing negative temperature coefficient of resistance (NTCR)-type nature of the material which also confirmed from conductivity analysis. The temperature dependence of σ_{dc} reveals an Arrhenius-type behavior with two activation energies, 0.98 eV in region I and 0.67 eV in region II. Studied sample's conduction is assured by Na$^+$ ions' hopping in tunnels and its mechanism was discussed.

Keywords: Sodium–magnesium orthophosphate; Raman; phase transition; NSPT model; sodium-ion conductivity.

1. Introduction

In the last few years, numerous research studies have emphasized on the phosphate-based materials, not only by understanding their wide range of variety but also by their different technological applications.[1–6] Particular interest has been devoted to the orthophosphate materials with formula ABPO$_4$ (A = Na, Li..... and B = Fe, Ni, Co, Mg.....) thanks to their attractive properties.[7–11] Among these properties, we can mention the optical and ferroelectric properties and also their excellent thermal stability, hydrolytic stability and charge stabilization.[12–14]

Moreover, the specific characteristic of the orthophosphate that comprehended a monovalent cation was also the researchers 'center of interest' thanks to their significant ionic conductivity and potential value as solid electrolytes for rechargeable "alkaline batteries".[15–17]

Diversity crystalline structures are a principal feature for this family of compounds that are controlled by the stereo-chemical behaviors of the A and B cations.[18–21] Among the different structures, we are interested in the olivine-type materials that possess a strong correlation between structural, physical and electrochemical properties.[22–24]

However, to our knowledge, no conductivity and vibrational behavior studies have been carried out in the title compound up to date. According to Alkemper and Fuess, it crystallized in orthorhombic symmetry with the P2$_1$2$_1$2$_1$ space group.[25]

The atomic arrangement is composed of chains of edge-sharing MgO$_6$ octahedral, which are cross-couped by the PO$_4$ groups building a 3D network. The perpendicular tunnels to the [0 1 0] direction contain octahedral coordinated Na$^+$ cations mobiles in these cavities (Fig. 1). It follows a transformation from α phase (α-NaMgPO$_4$) to the β phase (β-NaMgPO$_4$) around $T = 693$ K.[25]

As a continuation of our interest in the NaMgPO$_4$ compound, the impedance spectroscopy was made as a function of the temperature and frequency to evaluate the dielectric properties and to understand the conduction process in this material.

2. Experimental Procedures

The polycrystalline sample of NaMgPO$_4$ has been prepared using the standard solid-state reaction technique. The starting materials were Na$_2$CO$_3$, MgCO$_3$ and NH$_4$H$_2$PO$_4$ with a purity of 99.99%. These powders were mixed in stoichiometric ratio and were ground for 2 h in an agate mortar. The mixture the blend of these materials was gradually heated in
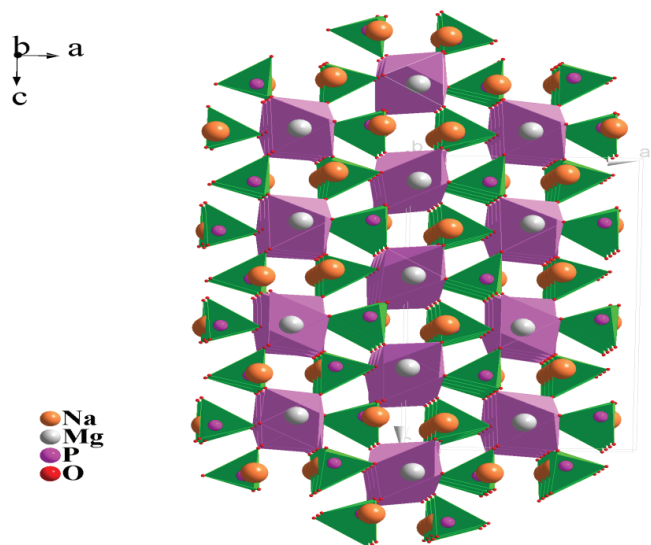
*Corresponding author.

Fig. 1.   Projection of the NaMgPO$_4$ structure along [0 1 0] direction.

Fig. 2.   X-Ray diffractogram of NaMgPO$_4$ compound at room temperature.

the beginning from the room temperature to 573 K to eject NH$_3$, H$_2$O and CO$_2$. The attained powder was hurried into cylindrical pellets of 8 mm diameter using 3 t/cm^2 uniaxial pressures and heated for 10 h at 973 K with a rate of 5°C/min. This process was remade recurrently with intermediary grindings in order to get the complete reaction and formation of a single-phase product.

X-ray powder diffraction pattern was registered using a Philips PW 1710 diffractometer in a wide range of Bragg angles (15° ≤ 2θ ≤ 60°) operating with Cu-Kα radiation ($\lambda_{K\alpha}$ = 1.5418 Å). The ceramic compound's unit cell parameters were fined by the least square method from the powder data.

The infrared spectrum of the ceramic NaMgPO$_4$ was registered at room temperature in an aide Perkin Elmer FTIR 100 between 400 and 1200 cm^{-1}.

Raman scattering measurements were investigated by a Horibe Jobin-Yvon T64000 spectrometer in the frequency interval of 15–1250 cm^{-1} with a resolve of 2 cm^{-1} in the temperature scale 633–753 K. The program LABSPEC5 software was employed for fitting the spectra with a combination of Lorentzian–Gaussian functions. The fitting procedure was carried out to interpret quantitatively the evolution of Raman bands as a function of the temperature.

The impedance spectroscopy measurements were performed in the frequency range from 200 Hz to 5 MHz with 10 points per decade at room temperature using an impedance analyzer (Tegam 3550). The electrical touches were effectuated by utilizing silver electrodes which were introduced on the two circular faces of the sample. The obtained powder was compressed using a 5 T/cm^2 uniaxial pressure. Impedance spectra's investigation and fitting with complex empirical functions were effectuated using the Zview software. Measurements were realized from 573 K to 723 K.
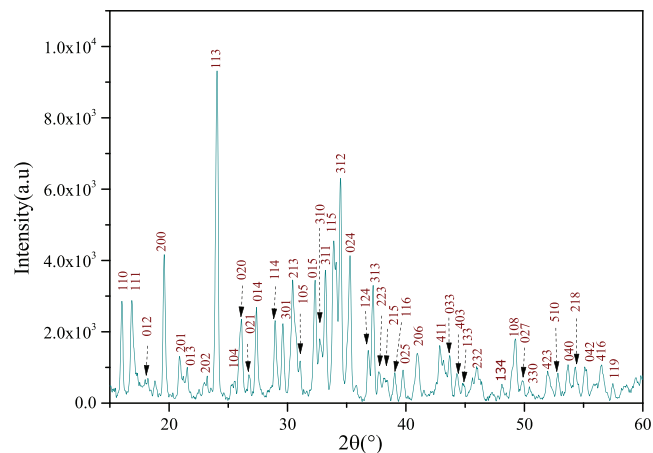
3.   Results and Discussion

3.1.   *Powder X-ray results*

Figure 2 plots the XRD pattern of NaMgPO$_4$ compound at room temperature. The detected XRD peaks were indexed to the orthorhombic symmetry with a P2$_1$2$_1$2$_1$ space group. The lattice parameters were fined using CELLREF software, were a = 8.828(2) Å, b = 6.821(2) Å, c = 15.250(4) Å and V = 918.3(4) Å^3 with valued standard deviation in parentheses. The purity of this material was confirmed by comparing the experimental patterns of the synthesized powder with the literature values.[25]

3.2.   *Vibrational analysis*

3.2.1.   *Vibrational study at room temperature*

Raman spectroscopy earned a key role in the cultural heritage for its exceptional skill to contribute to the structural properties of materials.

Vibration modes's analysis allows to identify the cations structural entourage, the lattice alteration and covalence.[26] To get details about the symmetry and the chemical bonding of the PO$_4$ group, it is important to investigate this compound's vibrational spectra. The free [PO$_4$] group has T_d symmetry and nine internal modes are distributed as follows:[27]

$$\Gamma T_d = A_1 + E + 2F_2.$$

A group theory analysis of the NaMPO$_4$ family of compounds was carried out in different studies.[28–30] In the title compound, C_s is the point symmetry of (PO$_4$)$^{3-}$ ions, which is less than the free ion's symmetry, thence the free ion's degeneracy of frequencies must be elevated as follows[31]:

$$A_1 \rightarrow A', E \rightarrow A' + A'', F_2 \rightarrow 2A' + A''.$$

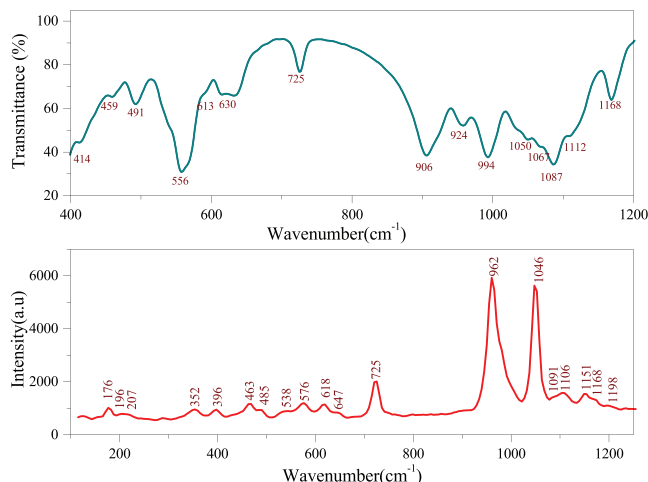The IR and Raman spectra for the title compound performed at room temperature between (400–1200) cm^{-1} and

Fig. 3. FTIR and Raman spectra of NaMgPO$_4$ recorded at room temperature.

(200–1300) cm^{-1}, respectively, are presented in Fig. 3. The ascriptions of the (PO$_4^{3-}$) mode are established on a compare with similar compounds[32–35] and the tentative attributions are listed in Table 1. The bands due to the symmetric and anti-symmetric stretching frequencies of (PO$_4^{3-}$) are in general detected in the 906–1198 cm^{-1} region. Further, the bands located in the 414–725 cm^{-1} region are assigned to the anti-symmetric and symmetric O–P–O bending modes. The external modes are situated below 400 cm^{-1}, where translations and librations of Mg and PO$_4$ ions are recorded.

3.2.2. *Temperature evolution in Raman spectra*

To gain more information on the compound dynamics and on the mechanism involved in the transition, we undertook a vibrational study using Raman scattering. Figure 4(a) shows the thermal evolution of Raman spectra of NaMgPO$_4$ in the spectral range [15–1250 cm^{-1}].

As the temperature increases, several changes in position and half-width are observed near the detected phase transition at 693 K. The occurrence of the wide and narrow modes simultaneously in the Raman spectra reveals the existence of order and disorder in the structure.[26] The spectra analysis (Figs. 4(b) and 4(c)) reveals that the important changes were detected in the external modes below 400 cm^{-1}. A large

change was detected for the peak at 106 cm^{-1}, where it broke into two bands near the phase transition (693 K). Another important change was observed near 48 cm^{-1} in the phase transition which is explained by a decrease of 8 cm^{-1} in the position. On the other hand, various important changes are observed in the asymmetric and symmetric O–P–O bending modes. The line at 458 cm^{-1}(δ_2) is divided into two components in the phase transition (693 K). The peak observed at 568 cm^{-1} (δ_4) is an increase in position by 2 cm^{-1} and in the half-width by 5 cm^{-1}. Whereas, the half-width of the band situated at 575 cm^{-1} (δ_4) is decreased by 7 cm^{-1}.

External modes and PO$_4$ deformation modes are the most sensible to the thermal effect. Splitting of those modes are the most characteristic of the phase transition. This implies the existence of some distortions of the PO$_4$ tetrahedral. The large size of Na cations in the conducting channel may lead to compression of PO$_4$ tetrahedral due to its relative size.[26]

The located bands between 900 and 1200 cm^{-1}, which were corresponding to the symmetric and asymmetric stretching modes, did not change significantly with the temperature; their position and half maximum underwent a weak change (a few cm^{-1}) which means that these modes are not directly influenced by the phase transition. From these observations, the changes around the temperature transition can be explained by a structural disorder effect, which is due to a strong tilt of the PO$_4$ and MgO$_6$ polyhedral.[36]

The splitting in some modes explains the disorder in NaMgPO$_4$ structure.

The phase transition in NaMgPO$_4$ is related to the rotation of MgO$_6$ and PO$_4$ polyhedral inversely, these rotations are due to the small cation displacements. The motion of sodium ions results in the heterogeneous spatial distribution of sodium ions around both magnesium and phosphorus units.[36]

3.3. *Dielectric relaxation behavior*

Solid's dielectric properties are very sensitive to the local field's partition within the sample. Dielectric properties' studies of the temperature and frequency dependence can expose effective detail on structural alterations, fault attitudes and transport phenomena.[36] The complex dielectric permittivity can be represented by the following equation:

$$\varepsilon^*(\omega,T) = \varepsilon'(\omega,T) - j\,\varepsilon''(\omega,T), \tag{1}$$

Table 1. Vibrational spectra data (cm^{-1}) and band assignments in NaMgPO$_4$ compound.

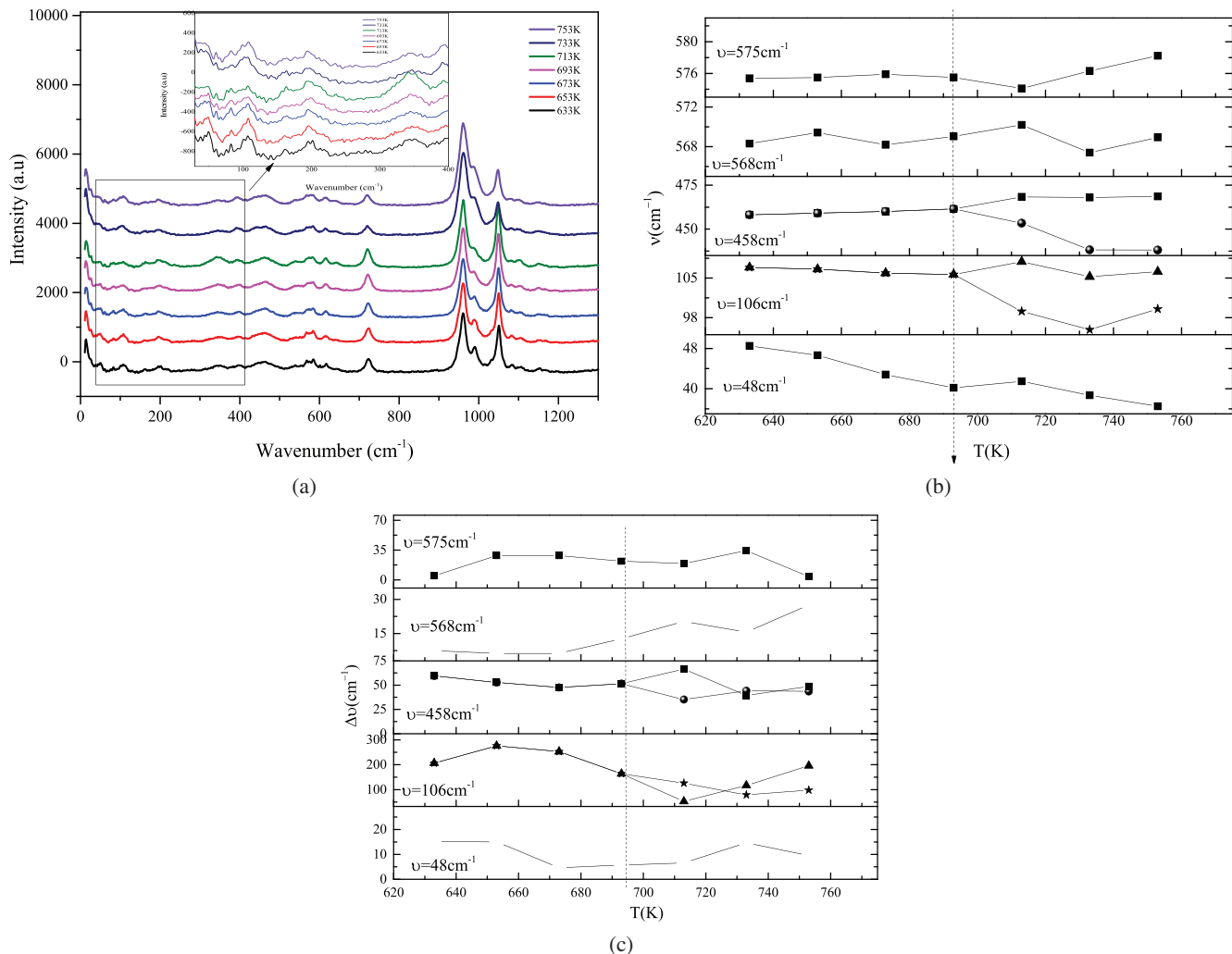| Raman wavenumber (cm^{-1})	IR wavenumber (cm^{-1})	Assignments
176; 196; 207; 352	—	Translations and librations of Mg and PO$_4$
396; 463; 485	414; 459	δ_s (PO$_4^{3-}$)
538; 576; 618; 647; 725	491; 556; 613; 630; 725	δ_{as} (PO$_4^{3-}$)
962	906; 924; 994	ν_s (PO$_4^{3-}$)
1046; 1091; 1106; 1151; 1168; 1198	1050; 1067; 1087; 1112; 1168	ν_{as} (PO$_4^{3-}$)

Fig. 4. (a) Temperature evolution of the Raman spectra in the 15–1250 cm⁻¹ frequency range; (b) and (c) Temperature dependence of the positions and of the half-width of the modes in the 35–600 cm⁻¹ spectral range.
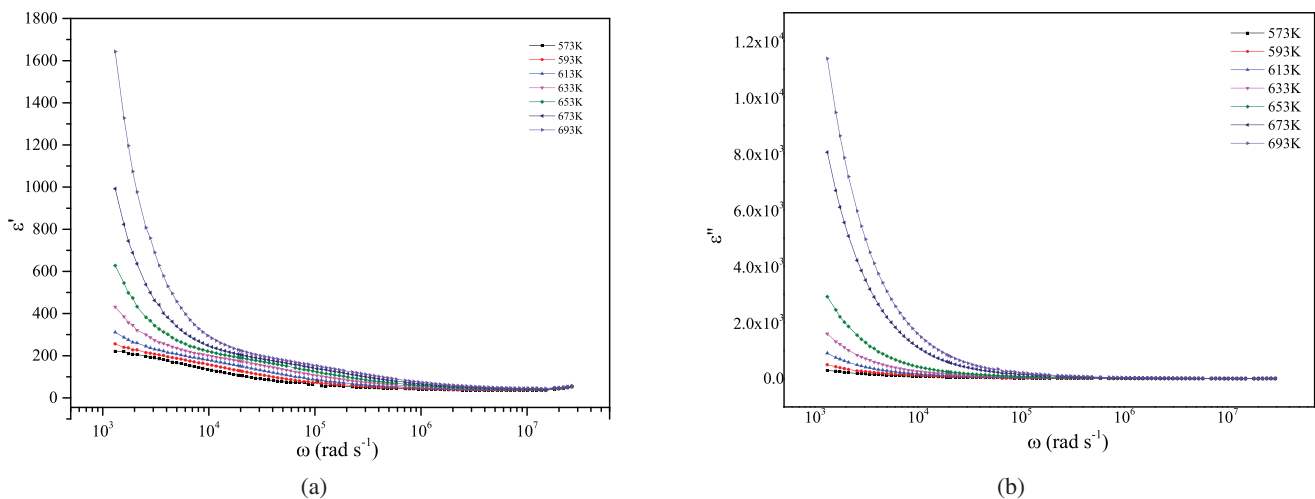

Fig. 5. Frequency dependence of ε' and ε'' at several temperature.

where ε' and ε'' are, respectively, the real and imaginary parts of the dielectric constant.

Variation of real ε' and imaginary ε'' parts of NaMgPO$_4$ ceramic according to the frequency at various temperatures is displayed in Fig. 5. The higher values of ε' and ε'' at low frequencies concede the synthetized material probably a suitable candidate for low frequency energy storage devices of the applied alternating electric field.[37] Afterwards, these dielectric constants' values reduce till they attain low values towards higher frequencies.

The scatter producing in the low-frequency region has been associated to this interfacial polarization. The electron swap causes electrons to move locally towards the electric field which polarizes the sample. By increasing the frequencies, the charge carriers reverse their orientation more frequently before reaching the grain boundary and, therefore, polarization decreases.[38]

This behavior is explained by the interfacial polarization theory provided by Maxwell.[39]

The temperature addiction of the real ε' and imaginary ε'' parts of the permittivity at divers frequencies is presented in Fig. 6. It is clear that at low frequency, ε' and ε'' values live constant. This can be explained that at low temperature, the charge carriers cannot follow the orientation.

Above $T = 633$ K, a swift jump of ε' and ε'' is detected. This skip is principally caused by the contribution of the migration polarization of Na$^+$ ions.

This behavior can be associated to thermal energy; the increase in temperature allows charge carriers to acquire thermal energy and align with the applied electric field which increases the dielectric constant.[40]

3.4. *Impedance analysis*

Impedance spectroscopy is an instructive and intense insight for investigating the corresponding electric and dielectric properties of materials and furthermore helps in understanding regarding several microstructures.[41] Although, to good approximation, such electrical specifications of a material can be closely depicted by an equivalent circuit which may be proposed by direct resultant impedance plots's consideration.

The Nyquist plots of the NaMgPO$_4$ ceramic at several temperatures are presented in Fig. 7. All the curves represented a trend to shift towards the abscissa to make up semicircles with their centers below the *x*-axis, having relatively smaller radii. The radii diminish with the temperature increase, showing the negative temperature coefficient of resistance (NTCR) behavior of the compound located with the semiconductors.[42] Such behavior shows a non-Debye type of relaxation and it also illustrates that there is a distribution of relaxation time in a state of a single relaxation time in the compound.

These plots are characteristic of typical polycrystalline materials with high resistive grain boundaries relative to grains.[43]

An equivalent circuit is useful to produce a complement picture of the system and build the structural–property relationship of the materials. Comparison of the complex impedance curves (symbols) along with the fitted data (lines) has been given in Fig. 7.

The associated equivalent circuit comprises of a parallel association of bulk resistance R_g and fractal capacity CPE$_g$ in series with a parallel combination of grain boundary resistance R_{gb} and fractal capacity CPE$_{gb}$ (Fig. 7).

The fractal capacitance's impedance CPE is described under the following form:

$$Z_{\text{CPE}} = [Q(j\omega)^\alpha]^{-1}, \qquad (2)$$

where Q shows the value of capacitance of the CPE element and deviation for the value of the pure capacitor.
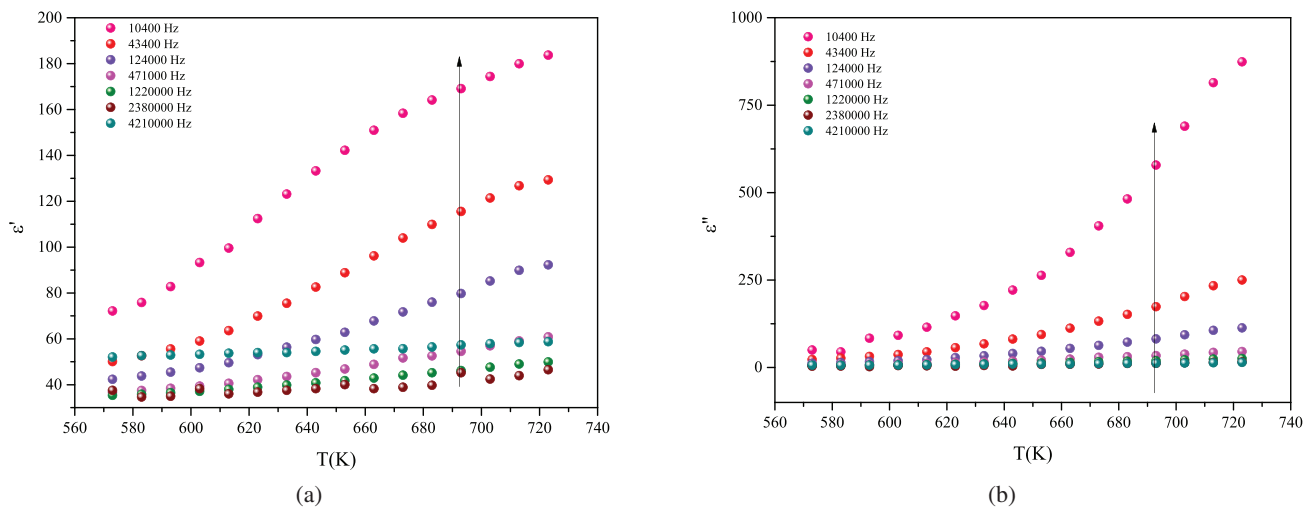

Fig. 6. Temperature dependence of ε' and ε'' at several frequencies.
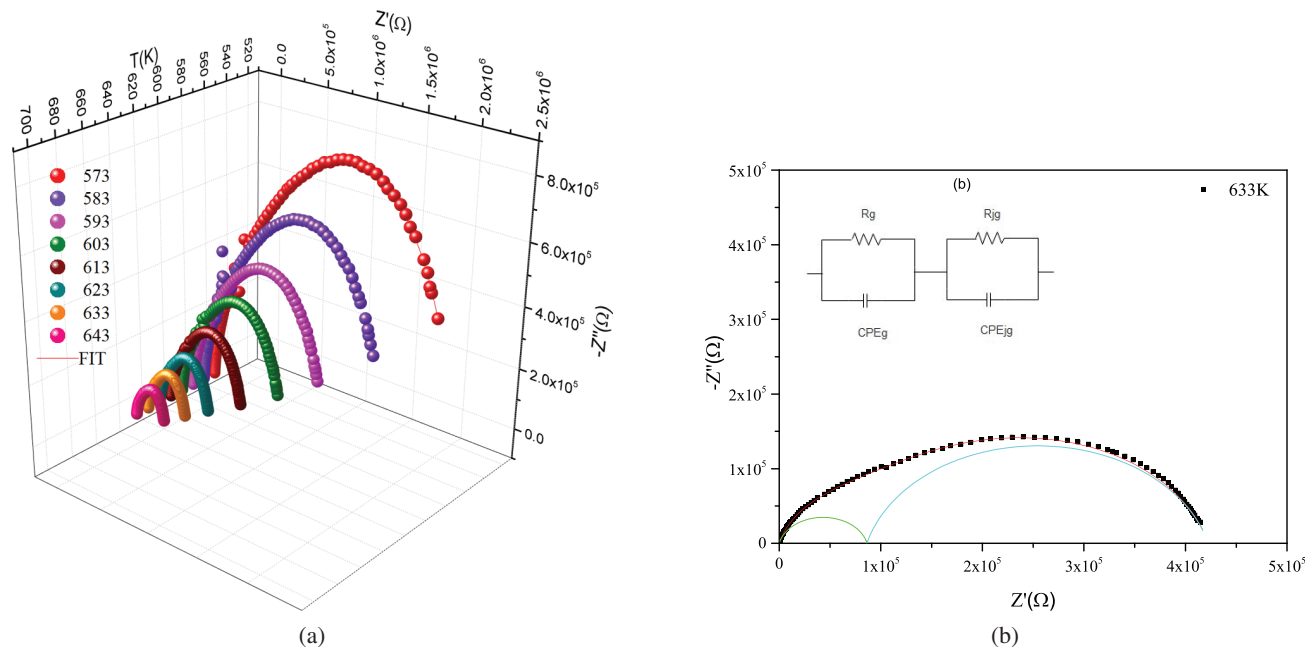
(a)

(b)

Fig. 7.   (a) Complex impedance spectra in the Nyquist plane and (b) electrical equivalent circuit.

From the parameter values excerpted from the equivalent circuit, the direct conductivities for the grain interior were defined at each temperature from the specified relation:

$$\sigma = \frac{e}{R_g S}, \qquad (3)$$

where e is the sample thickness, S is the area of the pellet and R_g is the bulk resistance value.

The thermal evolution of the grain σ_g and grain boundary conductivity σ_{gb} is reported in Fig. 8. Two regions are observed in this plot that follow the Arrhenius relation. The activation energies obtained by the linear fit are $E_{a1} =$

Fig. 8.   Dependence of Ln (σ_{dc}T) on temperature for the ceramic compound NaMgPO$_4$.

(0.98 ± 0.01) eV, $E_{a2} = (0.67 \pm 0.01)$ eV and $E_{a1} = (0.84 \pm 0.01)$ eV, $E_{a2} = (0.29 \pm 0.01)$ eV, respectively. This result confirms the phase transition detected by Raman spectroscopy. The decrease in activation energy may be related to increasing the degrees of freedom of the charge carrier when the temperature increases.

It is noticed that the conductivity of the sample increases with an increase in temperature, suggesting that the electrical conduction is a thermally activated process. This behavior can be attributed to several factors such as polarizability of sodium cation, mobility of charge carriers and the cross-section of the tunnels.[44]

3.5.   *Conductivity analysis*

The electrical conductivity σ_{ac} investigation is an important factor that exposes the powerful details about the transport phenomenon in materials. Count on the type of charge carriers (electron/holes or cations/anions) that govern the conduction procedure, the solids may distribute primarily as an electronic or ionic conductor. That way, the ac conductivity (σ_{ac})'s change as a function of frequency at various temperatures is shown in Fig. 9.

This plot shows two parts. The prime part is at low frequency described by a plateau region independently of frequency named σ_{dc}. While, the other part is at high frequency characterizing a dispersion region in which the conductivity increase is due to the mobility of charge carriers.

The slope change between dc and ac appears from a point named hopping frequency.[45] The plots reveal that the conductivity increases gradually with an increase in temperature. This observed increase at higher frequencies
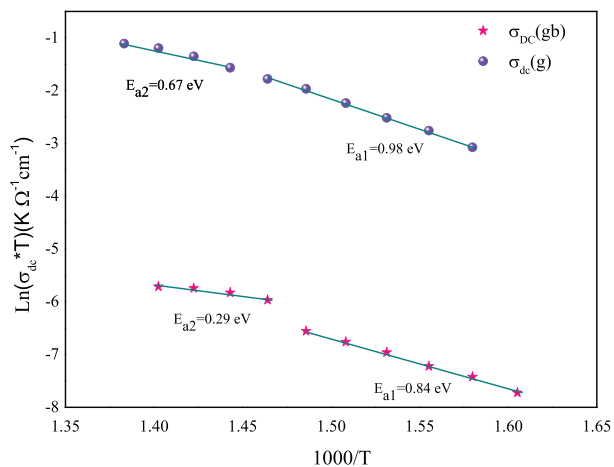
Fig. 9.   Frequency dependence of the ac conductivity at various temperatures.

Fig. 10.   Temperature dependence of the frequency exponent *s*.

is due to the thermally enhanced drift mobility of charge carriers.

These conductivity curves are scrutinized by the developed equation called the equation of Jonscher[46–48]

$$\sigma_{ac}\left(\omega\right) = \frac{\sigma_s}{1+\tau^2\omega^2} + \frac{\sigma_\infty \tau^2 \omega^2}{1+\tau^2\omega^2} + A\omega^s, \quad (4)$$

where σ_s is the conductivity at low frequencies, σ_∞ is the conductivity's evaluation at high frequencies, ω is the angular frequency and τ is the relaxation time. The exponent *s* presents cooperation between mobile ions with the neighboring lattices $(0 < s < 1)$ and *A* is a pre-factor that determines the strength of polarizability.

Thus, the extended oxygen vacancies density the space charges delivered on the grain boundaries can explain the increment of conductivity as the heating treatment.[49]

Depending on Jonscher, the base of the conductivity's frequency dependence consists of the relaxation phenomena that ensue from the moving charging operators. When a portable charge carrier jumps from its initial location to a fresh site, it keeps in a state of movement between two potential energy minima.

To explain a distinct conduction mechanism of ac conductivity, the temperature-dependent frequency exponent *s* (*T*) is relieved to detect some particular theoretical model in correspondence with the experimental proceeding.[50] In biography, the diverse theoretical models are based on the classical hopping of the charge carriers.

The frequency exponent *s* is obtained by fitting the ac conductivity using the above equation (Eq. (4)) which is plotted in Fig. 10 as a function of temperature. It is clear that *s* has a value between 0.42–0.59 and increases with increasing temperature. This result indicates that the nonoverlapping small polaron tunneling (NSPT) model is the most appropriate conduction mechanism.[51]
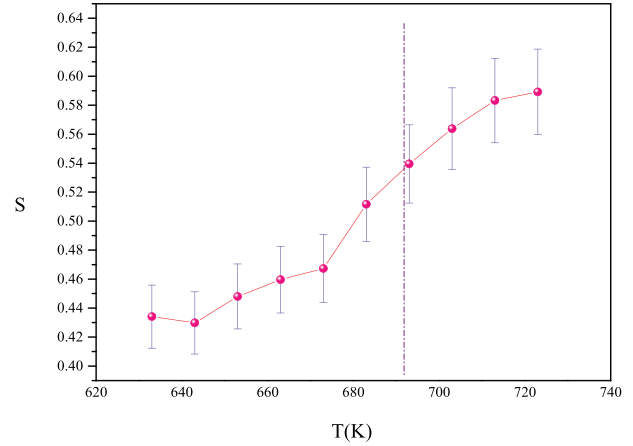
The small polaron is trained owing to the interaction between the electrons and the phonon cloud which was developed when the bringing atom was displaced from their equilibrium position and successfully screened at an electron's charge.

NSPT can be integrated in a covalent solid if the addition of a charge carrier to a site produces a large local lattice alteration.

For this model, the AC conductivity σ (ω) and the exponent *s* are presented as follows:[52]

$$\sigma(\omega) = (\pi e)^2 KT \alpha^{-1} \omega \left[N(E_F(T)) \right]^2 \frac{R_\omega^4}{12}, \quad (5)$$

$$s = 1 - \frac{4}{Ln\left(\frac{1}{\omega\tau_0}\right) - \frac{W_H}{TK}}, \quad (6)$$

where

$$R_\omega = \frac{1}{2\alpha}\left[Ln\left(\frac{1}{\omega\tau_0}\right) - \frac{W_H}{KT} \right], \quad (7)$$

where the reciprocal of Fröhlich coupling constant (α) is associated to the spatial extension of polaron; N (E_F) is the energy density of states near Fermi energy; the tunneling distance (R_ω) is strongly temperature dependence and W_H is the polaron hopping energy.

The ac conductivity is fitted from Eq. (5) and is given in Fig. 11 at different frequencies. The extracted ac parameters at various frequencies are collected in Table 2.

The density of state near Fermi level $N(E_F)$ decreases with the angular frequency increase. This result is followed in the literature.[53] The high values of N (E_F) recommend that the jumping between the pairs of sites commands the mechanism of charge transport in this compound.

Figure 12 represents the variation of the hopping distance R_ω at different temperatures. Such parameter increases with the increase in temperature. As the temperature of the material is rising, the polaron experience is thermally activated,
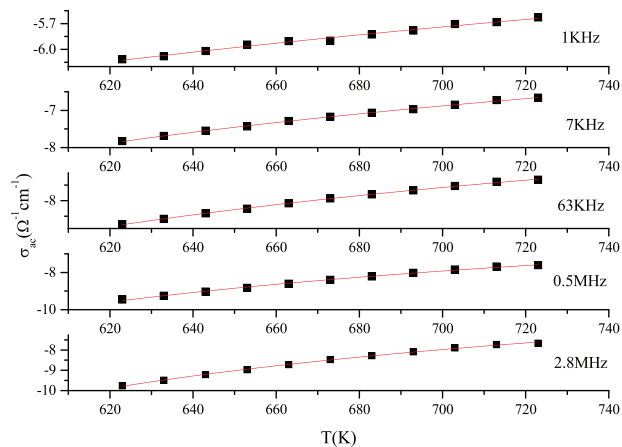
Fig. 11. Temperature dependence of the A.C. conductivity at different frequencies of NaMgPO$_4$ compound.

Fig. 12. Temperature dependence of the hopping distance R_ω.

Table 2. A.C. conductivity parameters for NaMgPO$_4$ compound at various frequencies.

Frequency (Hz)	$N(E_F)$ (m^{-3})	W_H (eV)
1060	1.49×10^{20}	0.85
7810	1.30×10^{20}	0.82
63600	4.81×10^{19}	0.67
569×10^3	2.25×10^{19}	0.54
288×10^4	8.18×10^{18}	0.27

(a)

(b)

Fig. 13. (a) Shape and dimensions of the (0 1 0) tunnel section and (b) Comparison of the coordination geometries around Mg cations.

resulting in the increase in the rate of interband interaction.[54] The extracted values of R_ω are of the order of the interatomic spacing. Similar results are given in the literature.[55] From R_ω values and the crystallographic properties by considering the Na–Na distance, we can deduce that the conduction process is ensured by the motion of small polarons between the defect states. This fact is due to the displacement of Na$^+$ ions along the [0 1 0] tunnels direction.

The NSPT model is suitable for highly localized polarons surrounded by a profound potential well. For that model, the produced thermal energy is too little to impose forthwith these polarons to hop beyond the potential well. In this latitude, the varied phonon helper proceeding assured a polaron jump between the adjacent neighbors.[56] When the temperature increases, the mobility of the charge carriers increases resulting the conductivity increase.

The size of the Na$^+$ cations fits well into the size of the channel, such phase is characterized by a high mobility of charge carriers. The localization of oxygen atoms is important in the structure. In the NaMgPO$_4$ structure (Fig. 2), the Mg atoms are arranged in three kinds of chains. Each kind of Mg^{2+} site has a different average distance between the cation and ligands (Fig. 13).[25] Variations in the local arrangements of ions create disorder cationic. Such disorder generates a small energy difference which is used by the polaron to hops
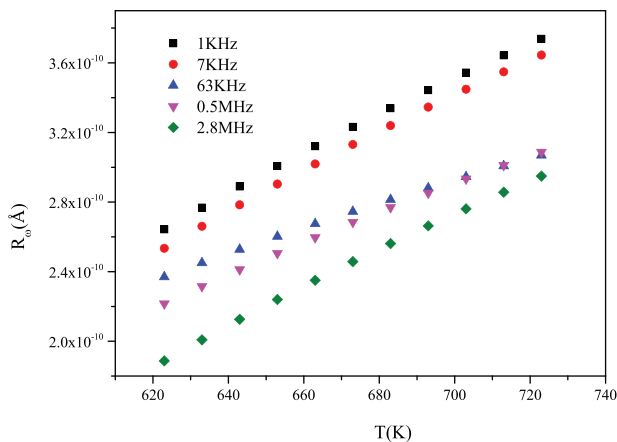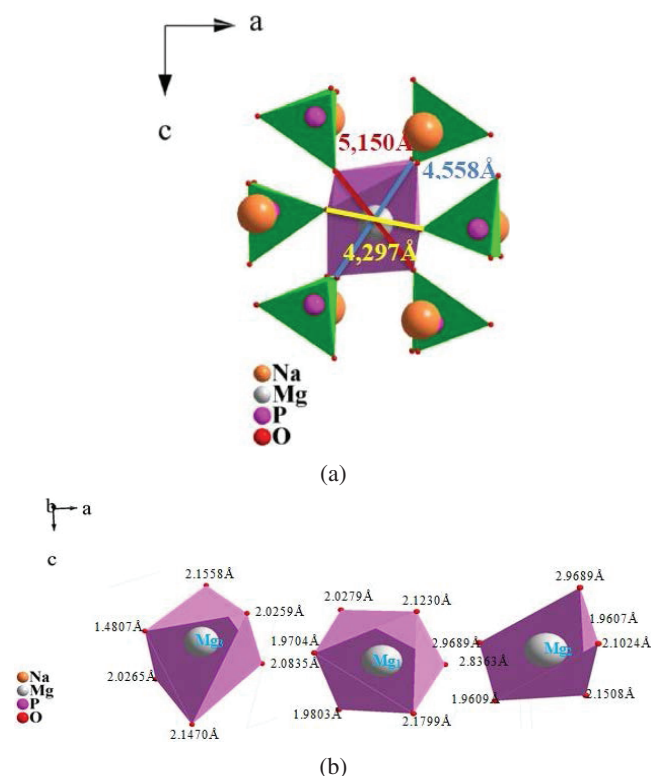
to suitable site. The energy exchange between polarons and disordered arrangement of atoms modified the localization length α^{-1}.[56]

The magnesium monophosphates, AMgPO$_4$ are a family with slightly different structure depending on the A$^+$ cation. Despite this, the morphology of these structures plays an important role in the rise in conductivity. The MgOn polyhedron is distorted in the reversed with increasing ionic radius giving rise to the stronger crystal-field strength.[57] This distortion introduces a reduction in the cross-section of the tunnels and an increase of the activation energy of the A+ hopping

which are seen in KMgPO$_4$[58,59] and RbMgPO$_4$[60] compounds. The distortion in oxygen bonds leads to high ionic diffusivity and rich electronic conductivity.

4. Conclusions

In this work, we have synthesized the monophosphate compound of the composition NaMgPO$_4$ by the classic ceramic method. It was found to crystallize in the orthorhombic symmetry with the P2$_1$2$_1$2$_1$ space group and assumes an olivine type structure. The sample undergoes a phase transition at $T = 693$ K which is confirmed by the Raman spectroscopy, conductivity and electrical studies.

The most changes of frequencies and bands width at the phase transitions are governed by the dynamic rotations of PO$_4$ and MgO$_6$ polyhedra. The electric permittivity had a dispersal in the low-frequency region and a reduction in the tendency with a further rise in the frequency. Nyquist plots revealed an appearance of two semicircle arcs, well modeled in terms of electrical equivalent circuit. The a.c. conductivity spectra are found to obey Jonscher's universal power law with s varying between 0.42 and 0.59. The NSPT model successfully explained the mechanism of charge transport in NaMgPO$_4$.

References

[1] J. H. Joshia, K. V. Vadhel, G. M. Joshic, M. J. Joshib, H. O. Jethvab and K. D. Parikhd, The complex impedance, dielectric relaxation, complex modulus and photoluminescence studies of pure and L-Methionine doped ammonium dihydrogen phosphate, *J. Chin. Phys.* **65**, 268 (2020).

[2] Fang-Fang. Chen, H. F. Li, X. R. Jia, Z. Y. Wang, Y. Y. Qin, X. Liang, W. Q. Chen and T. Qi. Ao, A quantitative prediction model for the phosphate adsorption capacity of carbon materials based on pore size distribution, *J. Electrochim. Acta* **331**, 135377 (2020).

[3] S. Ryu, J. E. Wang, J. H. Kim, R. Ruffo, Y. H. Jung and D. K. Kim, A study on cobalt substitution in sodium manganese mixed-anion phosphates as positive electrode materials for Na-ion batteries, *J. Power Sources* **444**, 227274 (2019).

[4] M. Srout, M. El Kazzi, H. Ben Youcef, K. M. Fromm and I. Saadoune, Improvement of the electrochemical performance by partial chemical substitution into the lithium site of titanium phosphate-based electrode materials for lithium-ion batteries: LiNi$_{0.25}$Ti$_{1.5}$Fe$_{0.5}$(PO$_4$)$_3$, *J. Power Sources* **461**, 228114 (2020).

[5] Y. Zhang, J. A. Alarco, J. Y. Nerkar, A. S. Best, G. A. Snook and P. C. Talbot, Nanoscale characteristics of practical LiFePO$_4$ materials - Effects on electrical, magnetic and electrochemical properties, *J. Mater. Charact.* **162**, 110171 (2020).

[6] O. Noureddine, S. Gatfaoui, Silvia. A. Brandan, A. Sagaama, H. Marouani and N. Issaoui, Quantum chemical calculations, spectroscopic properties and molecular docking studies of a novel piperazine derivative, *J. Mol. Struct.* **1207**, 127762 (2020).

[7] M. U. Kartin, K. M. S. G. Etheredge, G. L. Schimeka and Sh.-J. Hwu, Synthesis, structure, and magnetic properties of two quasi-low-dimensional antiferromagnets, NaMnAsO$_4$ and β-Na-CuPO$_4$, *J. Alloys Compd.* **338**, 80 (2002).

[8] A. Sun, F. R. Beck, D. Haynes, J. A. Poston, Jr. S. R. Narayanan, P. N. Kumta and A. Manivannan, Synthesis, characterization,

and electrochemical studies of chemically synthesized NaFePO$_4$, *J. Mat. Sci. Eng. B* **177**, 1729 (2012).

[9] M. Amer and P. Boutinaud, The doping sites in Eu^{2+}-doped AIBIIPO$_4$ phosphors and their consequence on the photoluminescence excitation spectra, *J. Solid State Chem.* **258**, 124 (2018).

[10] P. F. Henry, E. M. Hughes and M. T. Weller, Synthesis and structural characterisation of CsCoPO$_4$-ABW, *J. Chem. Soc. Dalton Trans.* 4, 555 (2000).

[11] L. Guan, Ch. Liu, X. Li, G. Jia, Q. Guo, Z. Yang and G. Fu, Synthesis and optical properties of KCaPO4:Eu^{2+} phosphor, *J. Mat. Res. Bull.* **46**, 1496 (2011).

[12] I. V. Korchemkin, V. I. Pet'kov, A. V. Markin, N. N. Smirnova and A. M. Kovalskii, Thermodynamic properties of caesium–cobalt phosphate CsCoPO$_4$, *J. Chem. Thermodyn.* **96**, 34 (2016).

[13] V. I. Pet'kov, I. V. Korchemkin, E. A. Asabina, A. R. Zaripov, V. S. Kurazhkovskaya, E. Yu. Borovikova and S. Yu. Stefanovich, *Russ. J. Inorg. Chem.* **57**, 1214 (2012).

[14] G. Nénert, J. Bettis, Jr. R. Kremer, H. Ben Yahia, C. S Ritter, E. Gaudin, O. Isnard and M.-H. Whangbo, Magnetic properties of the RbMnPO$_4$ Zeolite-ABW-Type Material: A frustrated Zigzag spin chain, *J. Inorg. Chem.* **52**, 9627 (2013).

[15] T. Dhanesh, A. Pulanchiyodan and T. S. Mailadil, Casting and characterization of LiMgPO$_4$ glass free LTCC tape for microwave applications, *J. Eur. Ceram. Soc.* **33**, 87 (2013).

[16] F. Zhou, K. Kang, T. Maxisch, G. Ceder and D. Morgan. The electronic structure and band gap of LiFePO$_4$ and LiMnPO$_4$, *J. Solid State Commun.* **132**, 181 (2004).

[17] M. S. Whittingham, Y. Song, S. Lutta, P. Y. Zavalij and N. A. Chernova, Some transition metal (oxy)phosphates and vanadium oxides, *J. Mater. Chem.* **15**, 3362 (2005).

[18] M. Luján, F. Kubel and H. Schmid, Some transition metal (oxy)phosphates and vanadium oxides, *J. Nat. Sci. B* **50**, 1210 (1995).

[19] R. Hammond, J. Barbier and C. Gallardo, Crystal structures and crystal chemistry of Ag XPO$_4$ (X=Be, Zn), *J. Solid. State Chem.* **141**, 177 (1998).

[20] L. Elammari, M. El Koumiri, I. Zschokke-Gränacher and B. Elouadi, Elaboration and non linear properties of ortho-phosphate solid solutions AiBII 1-xMII xPO$_4$ (AI = monovalent cation, BII & MII = divalent cations), *Ferroelectrics* **158**, 19 (1994).

[21] V. Koleva, T. Boyadzhieva, E. Zhecheva, D. Nihtianova, S. Simova, G. Tyuliev and R. Stoyanova, Precursor-based methods for low-temperature synthesis of defectless NaMnPO$_4$ with an olivine- and maricite-type structure, *J. Cryst. Eng. Commun.* **15**, 9080 (2013).

[22] M. D. Johannes, K. Hoang, J. L. Allen and K. Gaskell, Hole polaron formation and migration in olivine phosphate materials, *J. Phys. Rev. B* **85**, 115106 (2012).

[23] K. T. Lee, T. N. Ramesh, F. Nan, G. Botton and L. F. Nazar, Topochemical synthesis of sodium metal phosphate olivines for sodium-ion batteries, *J. Chem. Mater.* **23**, 3593 (2011).

[24] B. Louati and K. Guidara, Dielectric relaxation and ionic conductivity studies of LiCaPO$_4$, *Ionics* **17**, 633 (2011).

[25] J. Alkemper and H. Fuess, The crystal structures of NaMgPO$_4$, Na$_2$CaMg(PO$_4$)$_2$ and Na$_{18}$Ca$_{13}$Mg$_5$(PO$_4$)$^+$: New examples for glaserite related, *J. Non-crystalline Solids* **213**, 282 (1998).

[26] H. Bih, L. Bih, B. Manoun, M. Azdouz, S. Benmokhtar and P. Lazor, Raman spectroscopic study of the phase transitions sequence in Li$_3$Fe$_2$(PO$_4$)$_3$ and Na$_3$Fe$_2$(PO$_4$)$_3$ at high temperature, *J. Mol. Struct.* **936**, 147 (2009).

[27] M. E. Poloznikova and V. V. Fomichev, The vibrational spectra and characteristic features of the orthophosphates of Group I-III elements, *J. Russ. Chem. Rev.* **63**, 399 (1994).

[28] I. L. Botto and M. Vassallo, The vibrational spectrum of the NaZnPO$_4$ ferroelectric phase, *J. Mater. Sci. Lett.* **8**, 1336 (1989).

[29]Ch. M. Burba and R. Frech, Vibrational spectroscopic investigation of structurally-related $LiFePO_4$, $NaFePO_4$, and $FePO_4$ compounds, *J. Spectrochim. Acta A*. **65**, 44 (2006).

[30]A. Ajmi, M. Chemingui, A. Mahmoud, F. Boschini and A. Ben Rhaiem, Structural, vibrational spectroscopic, and electrical conduction mechanisms of α-$NaCoPO_4$ compound, *J. Ionics* **25**, 1091 (2018).

[31]A. Ait Salah, P. Jozwiak, K. Zaghib, J. Garbarczyk, F. Gendron, A. Maugerd and C. M. Julien, FTIR features of lithium-iron phosphates as electrode materials for rechargeable lithium batteries, *J. Spectrochim. Acta A* **65**, 1007 (2006).

[32]M. Rokita, M. Handke and W. Mozgawa, The $AlPO_4$ polymorphs structure in the light of Raman and IR spectroscopy studies, *J. Mol. Struct.* **555**, 351 (2000).

[33]V. I. Fomin, V. P. Gnezdilov, V. S. Kurnosov, A. V. Peschanskii, A. V. Yeremenko, H. Schmid, J.-P. Rivera and S. Gentil, Raman scattering in a $LiNiPO_4$ single crystal, *J. Low. Temp. Phys.* **28**, 203 (2002).

[34]O. García-Moreno, M. Alvarez-Vega, F. García-Alvarado, J. García-Jaca, J. M. Gallardo-Amores, M. L. Sanjuán and U. Amador, Influence of the structure on the electrochemical performance of lithium transition metal phosphates as cathodic materials in rechargeable lithium batteries: A new high-pressure form of $LiMPO_4$ (M = Fe and Ni), *J. Chem. Mater.* **13**, 1570 (2001).

[35]M. J. Bushiri, R. S. Jayasree, M. Fakhfakh and V. U. Nayar, Raman and infrared spectral analysis of thallium niobyl phosphates: $Tl_2NbO_2PO_4$, $Tl_3NaNb_4O_9(PO_4)_2$ and $TlNbOP_2O_7$, *J. Mater. Chem. Phys.* **73**, 179 (2002).

[36]A. C. Dhieb, A. Valkonen, M. Rzaigui and W. Smirani, Synthesis, crystal structure, physico-chemical characterization and dielectric properties of a new hybrid material, 1-Ethylpiperazine-1,4-diium tetrachlorocadmate, *J. Mol. Struct.* **1102**, 50 (2015).

[37]A. Hadded, J. Massoudi, E. Dhahri, K. Khirouni and B. F. O. Costa. Structural, optical and dielectric properties of $Cu_{1.5}Mn_{1.5}O_4$ spinel nanoparticles, *JRSC Adv.* **10**, 42542 (2020).

[38]M. S. Hossain, R. Islam and K. A. Khan. Electrical conduction mechanism and dielectric properties of vanadium doped ZnTe thin films, *J. Optoelectron. Adv. Mater.* **9**, 2192 (2007).

[39]E. M. El-Menyawy, H. M. Zeyada and M. M. El-Nahass, AC Conductivity and Dielectric Behavior of Silicophosphate Glass Doped by Nd2O3, *J. Solid State Sci.* **12**, 2182 (2010).

[40]A. Orliukas, A. Dindune, Z. Kanepe, J. Ronis, E. Kazakevicius and A. Ke_zionis, Synthesis, structure and peculiarities of ionic transport of $Li_{1.6}Mg_{0.3}Ti_{1.7}(PO_4)_3$ ceramics, *J. Solid State Ion.* **157**, 177 (2003).

[41]A. Badri, M. Jabli, M. Luisa López and M. Ben Amara, Synthesis, electrical and dye adsorption properties of $KZnFe(PO_4)_2$ zeolite type structure, *J. Inorg. Chem. Commun.* **110**, 107609 (2019).

[42]M. Benhaliliba, T. Asar, I. Missoum, Y.S. Ocak, S. Özçelik, C.E. Benouis and A. Arrar, Ac conductivity and impedance spectroscopy study and dielectric response of MgPc/GaAs organic heterojunction for solar energy application, *J. Phys. B* **578**, 411782 (2020).

[43]B. Alzahrani, S. Hcini, S. Mnefgui, A. Dhahri and M. L. Bouazizi, Ac conductivity and impedance spectroscopy study and dielectric response of MgPc/GaAs organic heterojunction for solar energy application, *J. Phase Transit.* **93**, 417 (2020).

[44]R. Chtourou, B. Louati and K. Guidara, AC and DC conductivity study of $KPb_4(PO4)_3$ compound using impedance spectroscopy, *J. Alloys Compds.* **727**, 771 (2017).

[45]T. Sahu and B. Behera, Dielectric and electrical study along with the evidences of small polaron tunnelling in Gd doped bismuth ferrite lead titanate composites, *J. Mater. Sci. Mater. Electron.* **29**, 7412 (2018).

[46]A. Despotuli and A. Andreeva, Maxwell displacement current and nature of Jonsher's universal, dynamic response in nanoionics, *J. Ion.* **21**, 459 (2015).

[47]Kh. Dhahri. Dielectric, ac conductivity and modulus studies of sol–gel $BaZrO_{2.9}$ compound, *J. Phase Transit.* **93**, 802 (2020).

[48]M. Salah, S. Azizi, A. W. Boukhachem, Ch. Khaldi, M. Amlouk and J. Lamloumi, Preparation and characterization of zinc sulfide thin films through the sulfuration of sprayed zinc oxide thin films, *J. Appl. Phys. A*. **125**, 615 (2019).

[49]Y.-M. Zhang, X.-Ch. Shen, Y.-C. Yan, G.-W. Wang, G.-Y. Wang, J.-Y. Li, X. Lu and X.Y. Zhou, *J. Rare Met.* **39**, 1256 (2020).

[50]A. Ghosh, Enhanced thermoelectric performance of ternary compound Cu_3PSe_4 by defect engineering, *J. Phys. Rev. B* **41**, 3 (1990).

[51]S. R. Elliott, A.c. conduction in amorphous chalcogenide and pnictide semiconductors, *J. Adv. Phys.* **36**, 135 (1987).

[52]S. Karmakar and Dh. Behera, Design and performance analysis of small scale parabolic trough solar collectors using sustainable materials, *J. Aust. Ceram. Soc.* (2020).

[53]S. Amhil, L. Essaleh, S. M. Wasim, G. Marín and E. Choukri, Low temperature analysis of the electrical conduction with the NSPT mechanism in p-$CuIn_3Se_5$, *J. Super Microstrut.* **119**, 194 (2018).

[54]H. E. Atyia and N. A. Hegab, Investigation of dielectric relaxation and a.c. conductivity of third generation multi-component $Ge10-xSe_{60}Te_{30}Sbx$ ($0 \le x \le 6$) chalcogenide glasses, *J. Optik* **127**, 6232 (2016).

[55]S. Hassairi, B. Louati and K. Guidara, Synthesis and characterisation of orthophosphate $KPbPO_4$ compound, *J. Alloys Compd.* **715**, 397 (2017).

[56]W. Khan, A. H. Naqvi, M. Gupta, Sh. Husain and R. Kumar, Small polaron hopping conduction mechanism in Fe doped $LaMnO_3$, *J. Chem. Phys.* **135**, 054501 (2011).

[57]G. Wallez, C. Colbeau-Justin, T. Le Mercier, M. Quarton and F. Robert, Crystal chemistry and polymorphism of potassium–magnesium monophosphate, *J. Solid State Chem.* **136**, 175 (1998).

[58]L. Miladi, A. Oueslati and K. Guidara, Phase transition, conduction mechanism and modulus study of $KMgPO_4$ compound, *J RSC Adv.* **6**, 83280 (2016).

[59]L. Miladi, A. Oueslati and K. Guidara, Vibrational spectroscopic and dielectric properties investigations of phase transitions in $KMgPO_4$ compound, *J. Mol. Struct.* **1148**, 404 (2017).

[60]R. AitBenhamou, G. Wallez, P. Loiseau, B. Viana, M. Elaatmani, M. Daoud and A. Zegzouti, Polymorphism of new rubidium magnesium monophosphate, *J. Solid State Chem.* **183**, 2082 (2010).